Journal of Materials Chemistry B

Accepted Manuscript

ROYAL SOCIETY OF CHEMISTRY

www.rsc.org/materialsB

Journal Name

ARTICLE

Enhancing performance of Mg–based implant material by introducing basal plane stacking faults

Yufeng Jiao,[ab] Jinghuai Zhang,*[a] Pengyu Kong,[cd] Zhongwu Zhang,[a] Yongbin Jing,[cd] Jinpeng Zhuang,[c] Wei Wang,[a] Li Zhang,[a] Chi Xu,[a] Ruizhi Wu[a] and Milin Zhang[a]

One of the keys to allowing Mg alloys served as biodegradable materials is how to balance their degradation behaviours and mechanical properties in physiological environment. In this study, a novel Mg–6Ho–0.5Zn alloy (wt.%) containing profuse basal plane stacking faults (SFs) is prepared. This newly-developed alloy with SFs exhibits uniform corrosion behaviour, low corrosion rate and high mechanical properties, as compared to the classic Mg-Ho based alloys (Mg–6Ho and Mg–6Ho–1.5Zn). Furthermore, the Mg–6Ho–0.5Zn alloy shows no significant toxicity to Saos-2 cells. An original uniform corrosion mechanism is proposed by combining the special defect structure, orientation of SFs and prompt effective corrosion film. The development of new microstructure for Mg-Ho based alloys with desirable corrosion performance has important implications in developing novel degradable Mg-based implant materials.

1. Introduction

Magnesium (Mg) alloys have attracted much attention for their potential use in a new stage as biodegradable medical implant materials due to some advantages, such as biodegradable behavior, biocompatibility, proper mechanical properties, close density and suitable elastic modulus with natural bones.[1-4] As a research hotspot, biodegradable Mg alloys have been studied for over a decade. However, up to now it is still hard to roll all the good qualities into one material and some critical issues have not been fully resolved.[5-7]

Control of corrosion rate and uniform corrosion behavior is a key issue for Mg alloys to serving as biodegradable materials. As one of the most electrochemically active metals, the main disadvantage of Mg alloys used as medical implants is their rapid corrosion behavior, even as the biodegradable implants.[8] The accelerated corrosion makes Mg alloys difficult to offer adequate mechanical support before complete restoration of organs. Also, the accumulation of hydrogen gas pockets during corrosion is also deleterious to the injured tissues.[9] Furthermore, Mg alloys tend to suffer inhomogeneous corrosion or severe pitting corrosion due to the non-uniform distribution of intermetallic particles or non-equilibrium grain boundaries.[10,11] Localized corrosion would cause an uncontrolled corrosion rate, stress concentration and rapid reduction in the mechanical integrities of Mg–based implanted devices during the degradation processes.[12] Therefore, a great effort has been devoted to the improvement of bio–corrosion properties. Some researchers[13-15] have been focusing on high purity, even ultrahigh purity Mg and Mg alloys to improve corrosion behavior for medical applications. On the other hand, many Mg–based alloy systems, including Mg–Ca,[16,17] Mg–Zn,[18,19] Mg–Sr,[20,21] Mg–Li,[22] Mg–Al and Mg–RE (rare earth),[7,23] have also been proposed for biomedical applications. Among them, Mg–RE alloy WE43 has already been used in clinical trials.[24] In recent years, the corrosion properties of many new biodegradable Mg–RE–based alloys have been reported, such as Mg–Y,[25–27] Mg–Gd,[28] Mg–Dy,[29,30] Mg–Nd,[31] Mg–Y–Zn,[32–35] Mg–Gd–Zn,[36,37] Mg–Dy–Zn[38] and Mg–Nd–Zn[39]. Zhang et al.[36] have reported that as–cast Mg–5Gd–1Zn–0.6Zr (wt.%) alloy with long period stacking ordered (LPSO) phase located near grain boundaries exhibits slower corrosion rate and more uniform corrosion morphology, as compared to the alloys without LPSO structure. Peng et al.[38] have reported that 14H LPSO structure in the grain interior is more effective for improving corrosion resistance than 18R LPSO structure at grain boundaries.

Compatibility between corrosion resistance and mechanical properties of biomedical magnesium alloys is required. In general, high alloying in Mg to introduce secondary phases is the effective way to enhance mechanical properties. On the other hand, however, secondary phases in the microstructure can also cause internal galvanic corrosion, and consequently accelerate corrosion rate and localized corrosion.[40] Therefore, it is still a challenge to design a alloy to enhance good corrosion behavior on the premise of high mechanical properties. Yang et al.[30] have reported that the

[a] Key Laboratory of Superlight Materials & Surface Technology, Ministry of Education, College of Material Science and Chemical Engineering, Harbin Engineering University, Harbin 150001, China.
[b] College of Materials Science and Engineering, Jiamusi University, Jiamusi 154007, China.
[c] Department of orthopedics, The Second Affiliated Hospital of Harbin Medical University, Harbin 150001, China.
[d] The Key Laboratory of Myocardial Ischemia, Harbin Medical University, Ministry of Education, Harbin 150001, China.
*Corresponding author. Tel.: +86-451-82569890; fax: +86-451-82569890
E-mail address: jinghuaizhang@gmail.com

Journal Name

ARTICLE

Table 1 Actual chemical compositions of pure Mg and the three alloys (wt.%)

Alloys	Ho	Zn	Fe	Ni	Cu	Mg
Pure Mg	/	0.001	0.003	0.002	0.006	Balance
Mg–6Ho	6.519	0.041	0.005	0.003	0.006	Balance
Mg–6Ho–0.5Zn	6.659	0.536	0.005	0.002	0.007	Balance
Mg–6Ho–1.5Zn	6.225	1.559	0.004	0.004	0.005	Balance

aged Mg–Dy–Gd–Zr alloy with nano–sized precipitates can obtain higher mechanica properties and lower corrosion rate than the as–cast alloy with micro-sized second–phase particles.

Based on the previous works, we have been focusing on designing a new microstructure for biodegradable Mg-based material. In recent years, some Ho-containing Mg alloys[41-43] as engineering structure materials with good mechanical and anti-corrosion properties have been reported. In this study, middle Ho content (6 wt.%) was selected in order to obtain a good balance of strength, ductility and anti-corrosion. Furthermore, a little Zn (0.5 or 1.5 wt.%) combined with Ho was also added to form a special structure in Mg alloys. In addition, it is well known that Ho has strong magnetic properties in comparison to other rare earths. Thus ,the implants containing Ho are expected to be visualized by MRI and X ray imaging.[2,6] In this work, we developed the Mg–6Ho–0.5Zn alloy with profuse basal plane stacking faults (SFs). The influence of SFs on the corrosion performance is clarified in detail, and relevant mechanisms are also discussed. The important discovery is that SFs are essentially different from common intermetallic compoundsThe formation of SFs in Mg–6Ho–0.5Zn alloy could promote to form uniform corrosion mode on the premise of low corrosion rate, high mechanical properties and low cytotoxicity.

2. Experimental procedures

2.1. Material preparation

High–purity Mg (99.98 wt.%), Zn (99.95 wt.%) and Mg–20 wt.% Ho master alloy were melted in an electric resistant furnace under protection of Ar atmosphere. Then the melt was poured into the cooling crystallizer at ~705 °C with a casting speed of 110 mm/min through the direct–chill semi–continuous casting process. Finally, the Mg–Ho–Zn alloy ingot witha diameter of 100 mm and length of ~1200 mm was obtained. After heat treatment at 500 °C for 12 h, the ingot was extruded at about 410 °C with an extrusion ram speed of 0.8 mm/s and an extrusion ratio of ~28. The actual chemical compositions were determined using inductively-coupled plasma (ICP) analysis. Considering that the corrosion behavior is also sensitive to the impurity of elements,[44] both the main alloying elements and the impurities were detected and listed in Table 1. pure Mg and Mg–Ho extruded rods were also prepared by the same method for comparison.

2.2. Microstructure characterization

The microstructure and phase composition of the alloys were characterized by scanning electron microscope (SEM) equipped with X-ray energy-dispersive spectrometer (EDS) and electron back-scattered diffraction (EBSD) system, transmission electron microscope (TEM) and X-ray diffractometer (XRD).

2.3. Mechanical tests

The tensile and compression directions of specimens were parallel to the extrusion direction. The tests were carried out on an Instron–5569 tester under an initial strain rate of 1×10^{-3} s^{-1}. The tension and compression tests can be referred to ASTM: E8 / E8M–13a and ASTM: E9-09, respectively. Each test was repeated for at least four times.

2.4. Electrochemical measurements

Potentiodynamic polarization measurements were performed in a standard three–electrode setup: a sample as the working electrode, a platinum plate as the counter electrode and a saturated calomel electrode as the reference electrode. The polarization curves were measured with a scan rate of 2 mV/s started from –300 mV relative to the open circuit potential and stopped at +300 mV relative to the open circuit potential. The electrolyte is the simulated body fluid (SBF). The ion concentrations in SBF are listed in Table 2. All specimen surfaces were ground successively to 2000 grit.

Journal Name

ARTICLE

Table 2 Detailed ion concentrations of the SBF

Components	Mass (g/l)
NaCl	8.035
$NaHCO_3$	0.355
KCl	0.225
$K_2HPO_4.3H_2O$	0.231
$MgCl_2.6H_2O$	0.311
c(HCl) = 1 mol/l	39 (ml)
$CaCl_2$	0.292
Na_2SO_4	0.072
TRIS	6.118

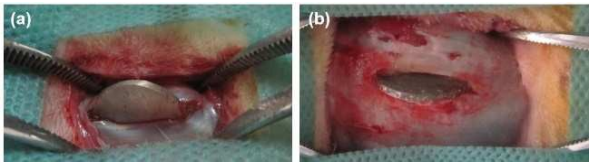

Fig. 1 Mg-6Ho-0.5Zn samples in the erector spinae of rabbit (a) before and (b) after in vivo corrosion.

2.5. In vitro corrosion tests

The in vitro corrosion behavior was evaluated by immersion tests in SBF according to ISO/FDIS 23317:2007(E). The temperature of SBF was maintained at 37±0.5 °C using a water bath. The SBF was buffered with TRIS–HCl and the pH was kept at ~7.4. During the immersion test, the SBF was refreshed every 36 h in order to avoid the effect of pH on the corrosion of Mg alloys. Before the test, the specimens were ground successively with SiC abrasive papers from 320 grit to 2000 grit and then cleaned with acetone and deionized water. Specimens were hung by cotton rope during an immersion experiment. The evolved hydrogen was collected by means of the funnel and the burette above the specimen. Initially the burette was full of solution, which was displaced by the evolved hydrogen, ensuring easy measurement of the corrosion rate of the specimen.

After each immersion test, the corrosion products of some specimens were cleaned by dipping in a solution of 200 g/L CrO_3, 10 g/L $AgNO_3$ and 20 g/L $Ba(NO_3)_2$, according to ISO 8407. Each immersion test was performed at least three times. The corroded surfaces were characterized by SEM with EDS, XRD and X–ray photoelectron spectroscope (XPS).

Corrosion rates, P_W, P_H and P_i, were obtained by using three measuring methods. P_W is the corrosion rate calculated from weight loss for 10 days immersion in SBF; P_H is the corrosion rate measured from hydrogen evolution for 10 days immersion in SBF; P_i is the corrosion rate evaluated by Tafel extrapolation from polarization curves measured after 1 h immersion in SBF. The calculation formulas used in this study are referred from literature[45,46] and listed as follows.

$$P_w=3.65\Delta W/\rho \quad (1)$$

$$P_H=2.279V_H \quad (2)$$

$$P_i=22.85i_{corr} \quad (3)$$

where ΔW is weight loss rate ($mg/cm^2/d$), ρ is the metal density (g/cm^3), V_H is the hydrogen evolution rate ($ml/cm^2/d$) and i_{corr} is the corrosion current density (mA/cm^2).

2.6. In vivo corrosion observation

6 adult male New Zealand rabbits of 2.5~3.0 kg in weight were used in this study, which were provided by the Animal Care Facilities of Harbin Medical University. Animals were generally anesthetized for surgery and the dorsum region was scrubbed with 25 g/L tincture of iodine and 70% ethanol. All rabbits were randomly assigned into two groups.Each rabbit was implanted two pure Mg or Mg–6Ho–0.5Zn alloy samples with a dimension of 15 mm in diameter × 1 mm thickness into the left and right erector spinae. The specimen surfaces were polished successively to 2000 grit. All animals received a subcutaneous injection of penicillin postoperation. Each group of rabbits was sacrificed 10 days after surgery. Fig. 1 shows the Mg-6Ho-0.5Zn samples in the erector spinae of rabbit before and after in vivo corrosion for 10 days. All procedures involving animals were approved by Harbin Medical University Ethics Committee for Animal Experiments and performed in accordance with the Guide for the Care and Use of Laboratory Animals published by the US National Institutes of Health. Finally, the corroded surfaces of samples were characterized by SEM with EDS.

2.7. Cytotoxicity test

Instead of the common murine fibroblast cells (L-929 cells), the human osteosarcoma cell line Saos-2 cells were adopted to evaluate the cell compatibility of pure Mg and Mg–6Ho–0.5Zn alloys by the MTT method, which were cultured in the Roswell Park Memorial Institute–1640 (RPMI–1640), 10% fetal bovine serum (FBS), 100 U/ml penicillin and 100 mg/ml streptomycin at 37 °C in a humidified atmosphere of 5% CO_2. Sample extracts were prepared according to ISO 10993–5:2009 for indirect contact assessments. Extracts were prepared with a surface area to extraction medium ratio of 1 ml/cm^2 in a humidified atmosphere with 5% CO_2 at 37°C for 1 day incubation. The concentrations of Mg, Ho and Zn ions in the extracts were measured by ICP-AES.

Journal Name

ARTICLE

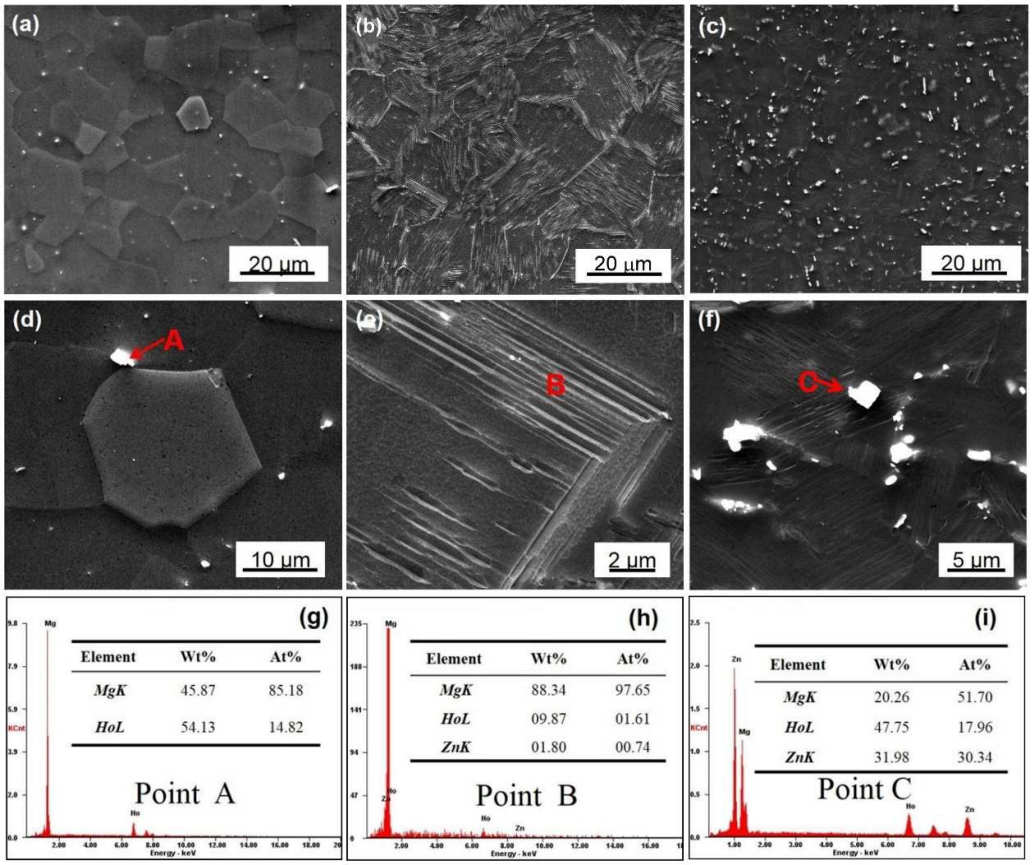

Fig. 2 Microstructures of the alloys and EDS results of the secondary phases: (a), (d) and (g) Mg–6Ho; (b), (e) and (h) Mg–6Ho–0.5Zn; (c), (f) and (i) Mg–6Ho–1.5Zn.

3. Results

3.1. Microstructural characterization

As revealed in Fig. 2(a), the as–extruded binary Mg–6Ho alloy is mainly composed of equiaxed α–Mg grains and a few secondary phase particles. With addition of small amounts of Zn, the microstructures of ternary alloys change obviously. When the content of Zn is 0.5 wt.%, as shown in Fig. 2(b), the additional profuse lamellae with a specific orientation in α–Mg grains are clearly visible, which distribute throughout the whole Mg matrix. However, excess Zn content (1.5 wt.%) causes the emergence of a large amount of secondary phase particles, though the α–Mg grains are more refined, as shown in Fig. 2(c). Fig. 2(d)–(i) shows the magnified SEM micrographs and EDS analyses of the three alloys, revealing the lamellae and secondary phases. . The small particles with most of the size less than 1 μm in Mg–6Ho alloy are identified as $Mg_{24}Ho_5$ (Fig. 2d and g).[47] Fig. 2(e) reveals the condition near the grain boundary in Mg–6Ho–0.5Zn alloy. From EDS analyses (Fig. 2h), the lamellae region is slightly rich in Ho and Zn elements. But, it needs to further confirm these lamellae. The size of most particles in Mg–6Ho–1.5Zn alloy is about 1–2 μm, and their composition is deduced as $Mg_3Zn_3Ho_2$ (W–phase) according to EDS analyses (Fig. 2f and i). It is reported that W–phase ($Mg_3Zn_3RE_2$) with face–centered cubic structure is the common secondary phase in as-cast or deformed Mg–Zn–RE (Y, Gd, and Er) alloys.[48-50]

The morphology and structure of the lamellae were further characterized by TEM. As shown in Fig. 3(a), the spacing of the parallel lamellae ranges from tens of nanometers to about 300 nanometers. The corresponding selected area electron diffraction (SAED) pattern (Fig. 3b) identifies it as a 2H–Mg crystal structure.

Journal Name

ARTICLE

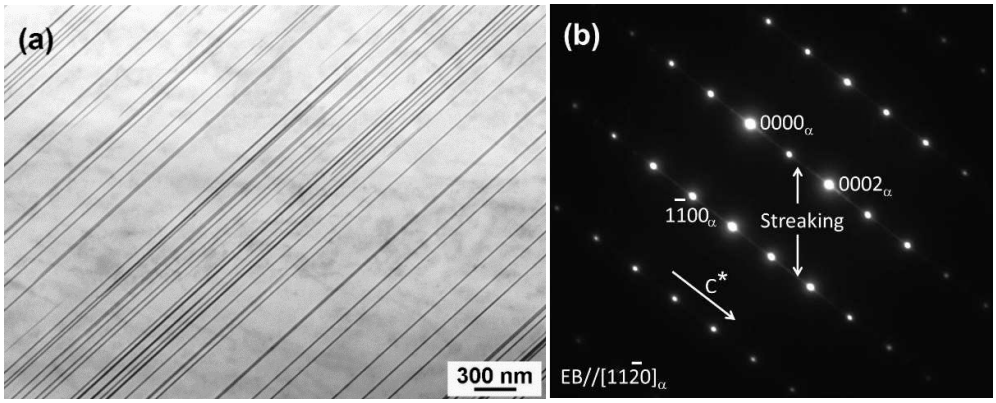

Fig. 3 (a) TEM image and (b) SAED pattern of SFs in Mg–6Ho–0.5Zn alloy.

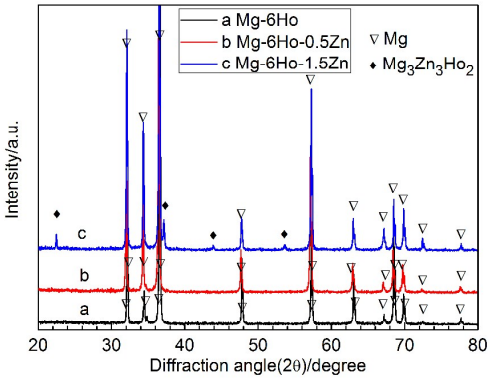

Fig. 4 XRD patterns of the three alloys.

More important, the formation of streaking rather than periodic extra spots between the diffraction spots along c–axis in SAED pattern verifies the existence of basal plane SFs instead of LPSO structure in Mg–6Ho–0.5Zn alloy.[51]

The phase composition of the three alloys is also detected by XRD analyses, as shown in Fig. 4.Only α–Mg matrix phase can be detected in the Mg–6Ho alloy because $Mg_{24}Ho_5$ particles are too few in number, which is in agreement with the SEM observation (Fig.2a). For Mg–6Ho–0.5Zn alloy, no secondary phase but α–Mg matrix phase can be detected from XRD pattern, which is consistent with the SFs formation determined by SAED pattern. For Mg–6Ho–1.5Zn alloy, diffraction peaks of both α–Mg phase and $Mg_3Zn_3Ho_2$ phase can be detected from XRD, confirming the results of SEM observation and EDS analyses. Thus, A conclusion can be drawn from the above results that a new Mg–6Ho–0.5Zn alloy with profuse nano–spaced SFs is prepared by combing the processes of direct–chill semi–continuous casting, proper heat–treatment and hot–extrusion. Consequently, the following studies in this paper will mainly focus on Mg–6Ho–0.5Zn alloy, and other alloys are tested just for comparison.

According to the recent reports, the crystal orientation (texture) not only influences mechanical properties but also corrosion.[52] Therefore, the anisotropy of wrought Mg alloys is also taken into consideration. Fig. 5 presents the EBSD results of the as–extruded Mg–6Ho–0.5Zn alloy. The results from Mg–6Ho binary alloy are also given in Fig. 5 for comparison. The inverse pole figures (IPF) (Fig. 5a and b) reveal that both the two as–extruded alloys have fully recrystallized microstructure, composing of relative uniform equiaxed grains. In addition, obvious colour difference of adjacent grains can be observed, which means a relatively large misorientation between these grains. Fig. 5(c) confirms that the two alloys have similar large angle grain boundaries after recrystallization. And the grain size difference is very small (Fig. 5d), that is, the average grain sizes for Mg–6Ho and Mg–6Ho–0.5Zn alloys are about 21 μm and 24 μm, respectively. The basal slip is the dominated deformation mode for Mg alloys at room temperature. As shown in Fig. 5(e), the basal slip Schmid factors along extrusion direction (ED) of Mg–6Ho binary alloy have high values with an average of 0.3047.For the Mg–6Ho–0.5Zn alloy with SFs, however, the basal slip Schmid factors are distributed relatively equally and their is an average value of 0.2289. The change of Schmid factor would affect the alloy performance to some extent. Ma et al.[53] have reported that RE elements Nd and Dy could weaken the basal texture of wrought magnesium. Accordingly, in this study the EBSD pole figure of as–extruded Mg–6Ho alloy exhibits a weak basal texture with basal plane deviating from the extrusion direction (Fig. 5f). It is worth noting that a similarly weak and random texture as that of Mg–6Ho alloy is also observed from the Mg–6Ho–0.5Zn alloy with SFs (Fig. 5g).

Journal Name

ARTICLE

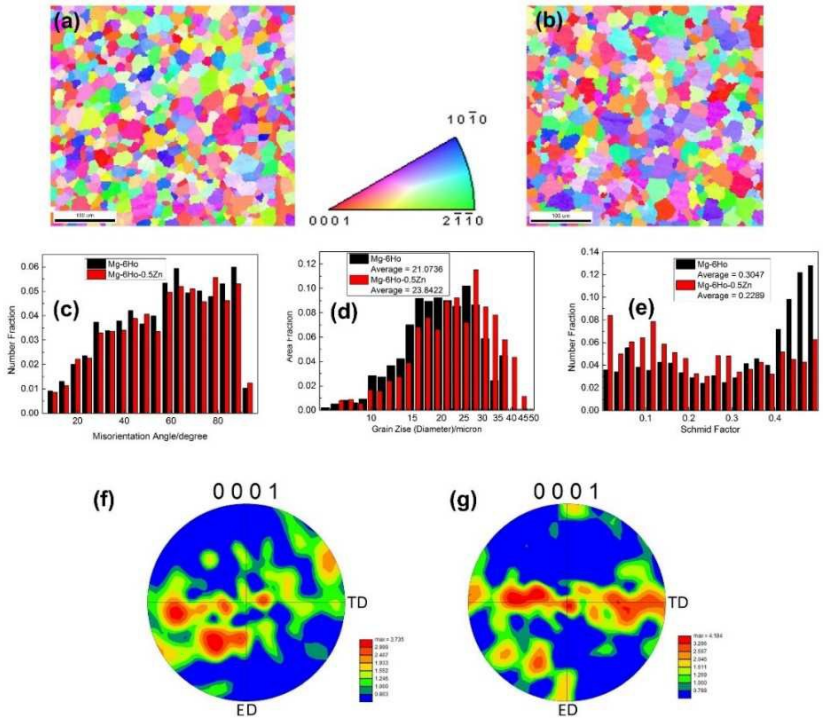

Fig. 5 EBSD analyses results for as–extruded Mg–6Ho and Mg–6Ho–0.5Zn alloys: (a) IPF map of Mg–6Ho; (b) IPF map of Mg–6Ho–0.5Zn; (c) misorientation angle distribution of two alloys; (d) grain size distribution of two alloys; (e) (0001)<11$\bar{2}$0> Schmid factor distribution along the ED of two alloys; (f) pole figure (0001) of Mg–6Ho; (g) pole figure (0001) of Mg–6Ho–0.5Zn.

Table 3 Mechanical properties of the as–extruded pure Mg, Mg–6Ho, Mg–6Ho–0.5Zn and Mg–6Ho–1.5Zn

Alloys	UTS (MPa)	TYS (MPa)	ε_T(%)	UCS (MPa)	CYS (MPa)	ε_C(%)
Pure Mg	174±5	75±3	8±1	297±5	56±2	26±1
Mg-6Ho	258±5	157±5	32±1	386±4	136±5	37±1
Mg-6Ho-0.5Zn	304±5	203±5	24±1	405±4	159±5	28±1
Mg-6Ho-1.5Zn	322±5	210±4	31±1	423±4	175±5	20±1

3.2. Effect of SFs on mechanical properties

As expected, pure Mg exhibits both low tensile strength and ductility (Table 3). With addition of Ho, tensile properties of the Mg–6Ho binary alloy are improved efficiently. It is worth noting that when little Zn (0.5 wt.%) is added into the binary alloy, the tensile strength increases significantly again along with the formation of profuse SFs in Mg–6Ho–0.5Zn alloy. The tensile yield strength (TYS), ultimate tensile strength (UTS) and elongation (ε_T) for Mg–6Ho–0.5Zn alloy are 203 MPa, 304 MPa and 24%, respectively. This indicates that the strength and ductility of Mg–6Ho–0.5Zn alloy are qualified to serve as a biodegradable material according to Erinc et al..[54] The higher tensile properties are obtained from Mg–6Ho–1.5Zn alloy due to the integrative effect of finer grain size and formation of SFs and W–phase. Nevertheless, W–phase particle is not a desired strengthening source due to its harmful effect on the corrosion rate and mode for biodegradable Mg alloys. Moreover, Mg–6Ho–0.5Zn alloy also exhibits the high compression yield strength (CYS), ultimate

Journal Name

ARTICLE

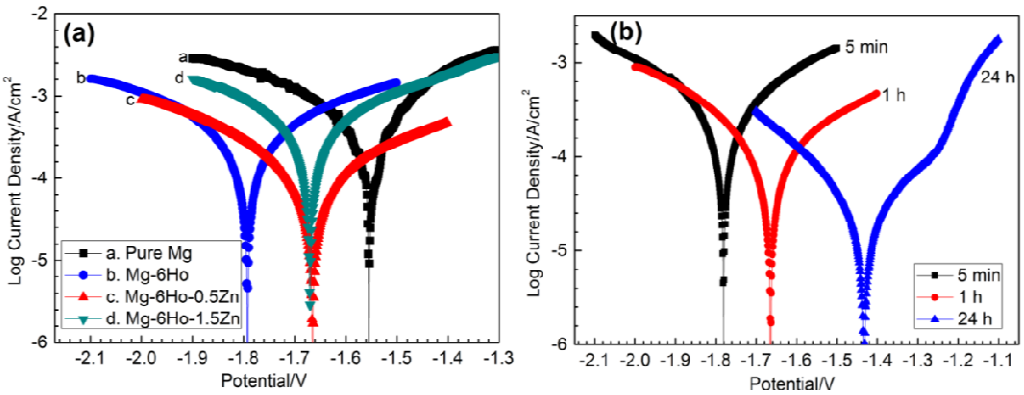

Fig. 6 (a) Polarization curves of the alloys after 1 h immersion in SBF; (b) polarization curves of Mg–6Ho–0.5Zn alloy for different immersion times in SBF.

Table 4 Measurements related to corrosion rate in SBF at 37°C. V_H and ΔW were measured using 240 h (10 days) immersion. Tafel extrapolation evaluated i_{corr} from polarization curves measured after 1 h immersion

Alloys	ΔW (mg/cm^2/d)	P_W (mm/y)	V_H (ml/cm^2/d)	P_H (mm/y)	i_{corr} (mA/cm^2)	P_i (mm/y)
Pure Mg	0.076	0.16	0.08	0.18	0.399	9.13
Mg-6Ho	0.845	1.75	0.7	1.79	0.202	4.64
Mg-6Ho-0.5Zn	0.121	0.25	0.12	0.27	0.080	1.85
Mg-6Ho-1.5Zn	1.358	2.80	1.26	2.95	0.319	7.38

compression strength (UCS) and compression ductility (ε_C) (Table 3).

3.3. Effect of SFs formation on electrochemical behavior

The corrosion resistance of these alloys was firstly evaluated using potentiodynamic polarization tests. Fig. 6(a) shows the polarization curves of the samples after 1 h immersion in SBF. It can be seen that addition of Zn in Mg–6Ho alloy shifts the corrosion potential to more positive values. Generally, the cathodic polarization curves mainly represent the cathodic hydrogen evolution by β–phase, while the anodic ones represent the dissolution of α–Mg.[55] According to Fig. 6(a), in the cathodic parts, the current density of Mg–6Ho–1.5Zn alloy is higher than those of Mg–6Ho and Mg–6Ho–0.5Zn alloys for all the time. It indicates that the cathodic hydrogen evolution from W–phase is kinetically easier and has lower overpotential on Mg–6Ho–1.5Zn alloy than Mg–6Ho and Mg–6Ho–0.5Zn alloys. In the anodic parts, Mg–6Ho–0.5Zn alloy has lower current density than other two alloys. It suggests that the formation of SFs makes anodic dissolution less active. Overall, the electrochemical corrosion behavior at short time suggests that Mg–6Ho–0.5Zn alloy with SFs has better corrosion resistance among the three alloys. Regarding to pure Mg, although its corrosion potential is more positive, its current density is the highest. The reason for this phenomenon may be that the corrosion film of pure Mg has the least corrosion resistance, thus the electrochemical corrosion is fast for pure Mg in a short–time test, though its more positive potential suggests its low corrosion tendency and may ensure a low corrosion rate for a long–term test. Hence here, it must be recognized that the electrochemical technique might not give reliable values for Mg corrosion.[46,55,56]

Journal Name

ARTICLE

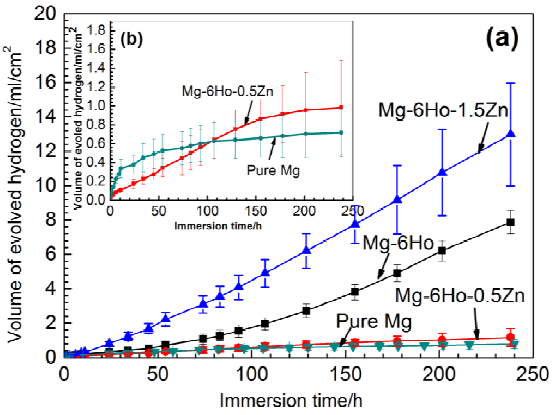

Fig. 7 (a) and (b) Hydrogen evolution volume curves as a function of immersion time in SBF

Fig. 6(b) shows polarization curves of Mg–6Ho–0.5Zn alloy samples with different immersion times before electrochemical tests. The result indicates that the corrosion potential moves to the positive direction and the corrosion current density decreases with increasing immersion time, which reveals the gradual improvement of corrosion resistance. The compared result suggests that a compact and stable corrosion product layer would be gradually formed on Mg–6Ho–0.5Zn alloy with SFs during the immersion in SBF.

3.4. Effect of SFs formation on corrosion rate in SBF

The corrosion performance studied by immersion tests reveals clear difference between Mg–6Ho–0.5Zn alloy and reference alloys. Fig. 7(a) and (b) show the hydrogen evolution during immersion in SBF at 37±0.5°C for 10 days. As expected, the high–purity Mg maintains a low hydrogen evolution rate during the immersion time compared with the three alloys (Fig. 7a). But it is noted from Fig. 7 (b) that at the initial stage the hydrogen evolution rate of high–purity Mg is higher than that of Mg–6Ho–0.5Zn alloy, which is consistent with result of potentiodynamic polarization test shown in Fig. 6(a). Most importantly, the investigated alloy, Mg–6Ho–0.5Zn alloy with SFs, shows a similarly low corrosion performance as that of the reference high–purity Mg.

Table 4 shows a comparison of the corrosion rates in the same units (mm/y) by three techniques of weight loss, hydrogen evolution and Tafel extrapolation of polarization curves. The simplest and most reliable and fundamental measurement of the corrosion rate is the alloy weight loss rate.[43] For Mg–6Ho–0.5Zn alloy with SFs, the corrosion rate is 0.25 mm/year after static immersion for 10 days, which is close to that of high–purity Mg (0.16 mm/year) and just ten percent of that of Mg–6Ho–1.5Zn alloy. It is important to note that the low corrosion rate of Mg–6Ho–0.5Zn alloy with SFs in SBF meets the performance criterion of Mg alloys as biomaterials suggested by Erinc et al..[51]

From Table 4, it can be seen that a good agreement is achieved between the low corrosion rates evaluated from the hydrogen evolution rate and that from the weight loss rate, as expected from the review of Song and Atrens.[43,52] While for all four materials, there is a large deviation for the corrosion rate determined from Tafel extrapolation compared with the weight loss rate, which is also in agreement with the observation of the review of Song and Atrens.[43,52] Therefore, Atrens[43] strongly recommended that for research that used Tafel extrapolation to elucidate corrosion of Mg, it should be complemented by two of the three other simple measurement methods: (a) weight loss rate, (b) hydrogen evolution rate, and (c) rate of Mg^{2+} leaving the metal surface. In this work, the corrosion rates from H_2 collection and weight loss is the average value of long–term tests (10 days), while the corrosion rate from polarization curves is the value of short–term tests (after immersion
for 1 h). Therefore, maybe the time is one of the effect factors, which is supported Fig. 7 (b). The detailed analyses and reasons were given by Song[52] and Atrens.[43] Shi and Atrens[53] have also reported that the correspondence can be attained for an experimental arrangement of simultaneous measurement of polarization curves and hydrogen evolution.

3.5. Effect of SFs formation on corrosion mode and corrosion products

The uniform corrosion mode is also crucial for biodegradable Mg alloys to extend their load–bearing period, and it seems more difficult to achieve without sacrificing other performances. Fig. 8 shows the surface morphologies of the three alloys after immersing in SBF for 5 days and then removing the corrosion products, demonstrating that the corrosion attacks on the three alloys are quite different. As shown in Fig. 8(a), the corrosion attack on the surface of Mg–6Ho alloy is inhomogeneous and a typical filiform corrosion clearly occurs. Filiform corrosion has also been observed in other Mg alloys,[40,54,55] and Liu et al.[55] have ever proposed a formation mechanism for Mg filiform corrosion. However, for the SFs–containing Mg–6Ho–0.5Zn alloy, the corroded surface is very smooth and homogeneous and no any pit or filiform corrosion can be observed after the immersion, as shown in Fig. 8(b). From the magnified image (Fig. 8c), it can be seen that the corrosion develops merely along the length direction of SFs inside of a α–Mg grain, and the SFs with different orientation in different grains effectively prevent corrosion from further extending to the neighboring grains. As expected, the typical pitting corrosion is found on the surface of Mg–6Ho–1.5Zn

alloy with profuse W–phase particles with size of 1–2 micrometers (Fig. 8d). The presence of W–phase particles would accelerate the extent of micro–galvanic corrosion and be responsible for the severe pitting corrosion. A comparison of the corrosion morphologies demonstrates that the corrosion modes of Mg–6Ho, Mg–6Ho–0.5Zn and Mg–6Ho–1.5Zn after immersion in SBF for 5 days are filiform corrosion, uniform corrosion and pitting corrosion, respectively, which just represent three typical corrosion mechanisms for Mg alloys.

Fig. 9 shows the surface morphologies after 10 days immersion in SBF and removing the corrosion products. For Mg–6Ho alloy, the filiform corrosion is replaced by the severe localized corrosion after a longer immersion time, as shown in Fig. 9(a) and (d). While for the Mg–6Ho–0.5Zn alloy with SFs the corrosion surface is smooth and uniform (Fig. 9b and e), which is just the desired surface structure. Therefore, SFs play a very important role in forming the typical uniform corrosion behavior and lower corrosion rate. For the Mg–6Ho–1.5Zn alloy with W–phase,

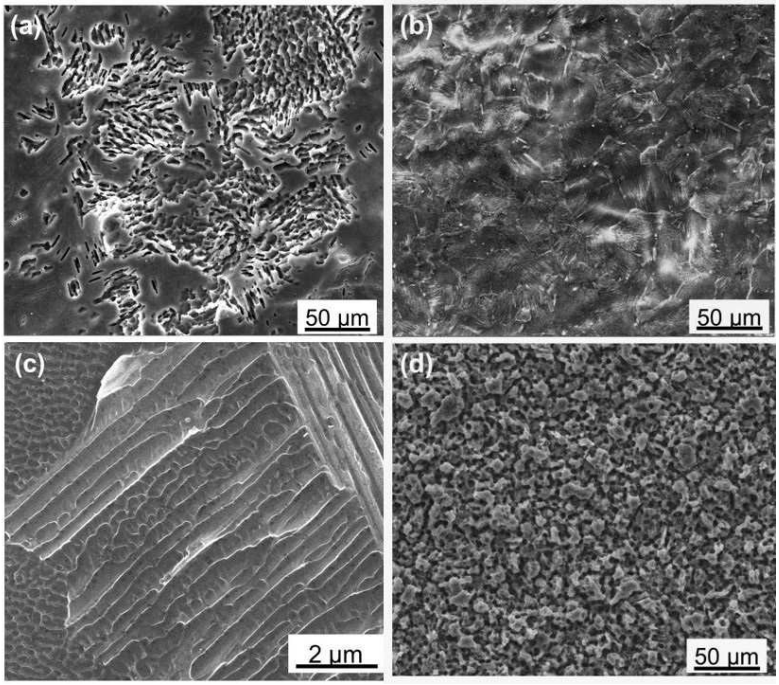

Fig. 8 SEM images showing the surface morphologies of the three alloys after 5 days static immersion in SBF solution at 37°C: (a) Mg–6Ho; (b) and (c) Mg–6Ho–0.5Zn; (d) Mg–6Ho–1.5Zn.

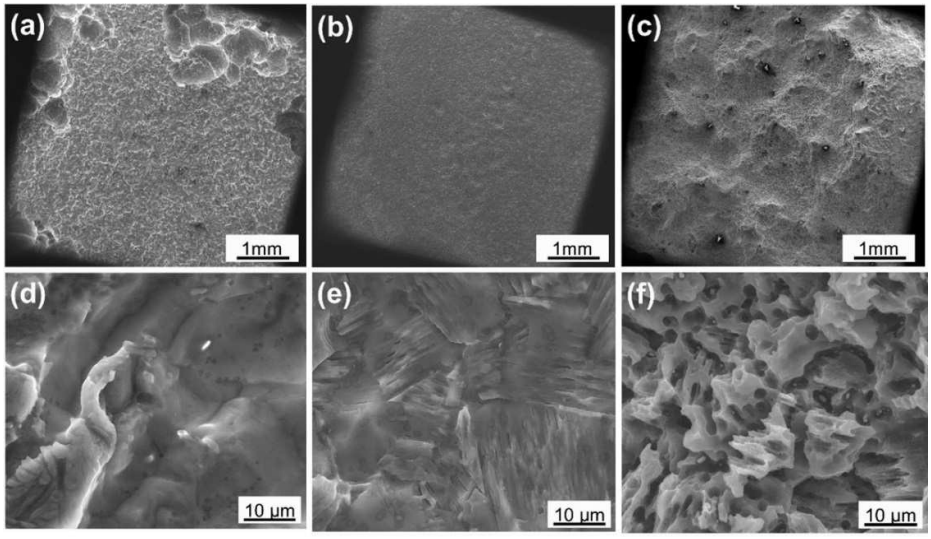

Fig. 9 SEM images showing the surface morphologies of the three alloys after 10 days static immersion in SBF solution at 37°C: (a) and (d) Mg–6Ho; (b) and (e) Mg–6Ho–0.5Zn; (c) and (f) Mg–6Ho–1.5Zn.

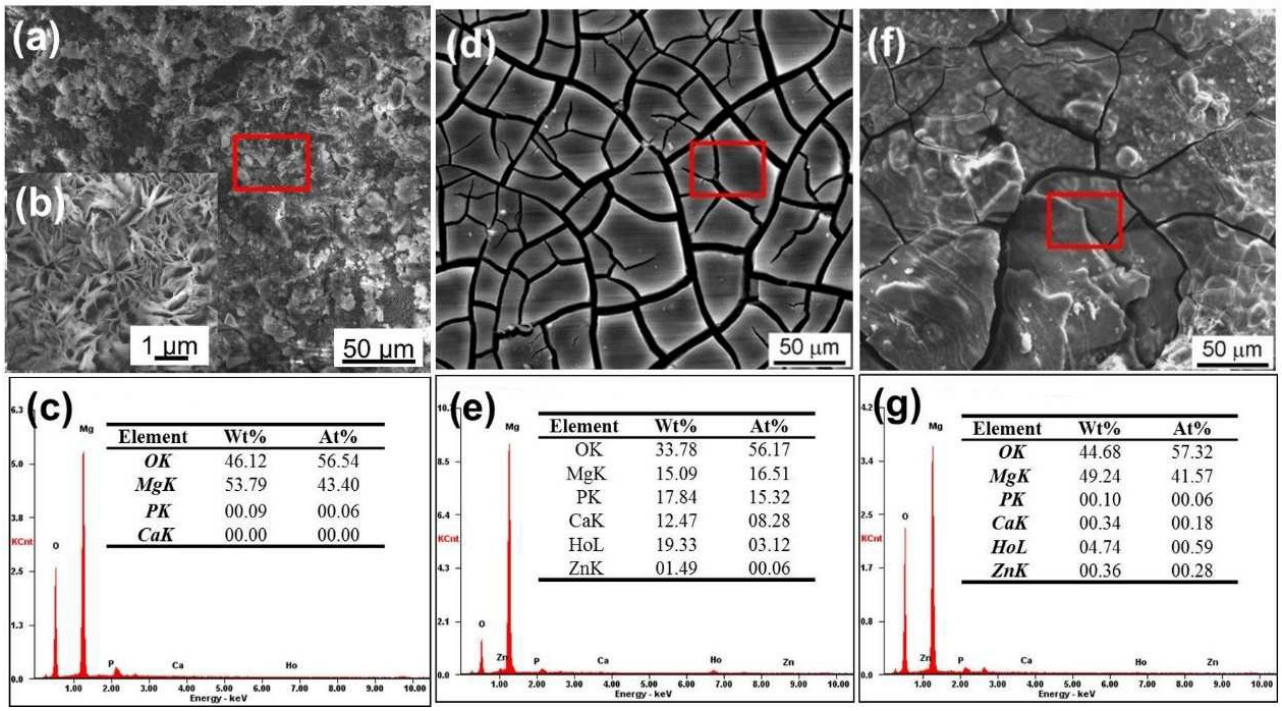

Fig. 10 SEM images and EDS analyses of the corrosion product layers after static immersion in SBF solution at 37°C for 10 days: (a), (b) and (c) Mg–6Ho; (d) and (e) Mg–6Ho–0.5Zn; (f) and (g) Mg–6Ho–1.5Zn. The red boxes are the regions detected by EDS.

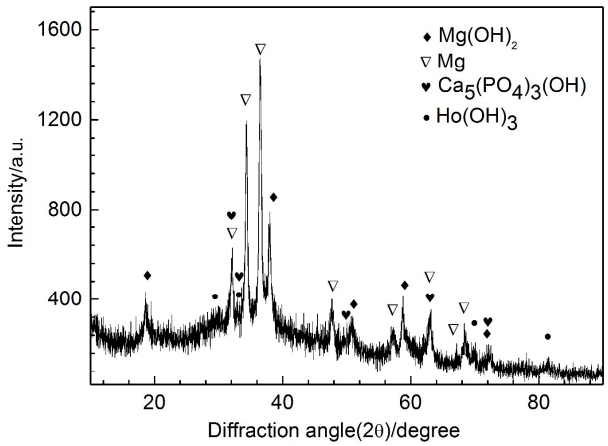

Fig. 11 XRD pattern of corrosion products powders stripped from the surface of Mg–6Ho–0.5Zn alloy after immersion in SBF for 10 days.

the severe pitting corrosion has caused the wavy surface, as shown in Fig. 9(c). The residual W–phase particles can be found at the bottom of pits (Fig. 9f).

The feature of corrosion layer also plays an important role in determining the corrosion resistance as well as the biocompatibility of Mg alloys. Fig. 10 shows the corrosion products of the three alloys after immersion in SBF for 10 days, demonstrating that both the morphology and chemical composition of the three corrosion films are quite different. The corrosion film of Mg–6Ho alloy seems to be thick but loose (Fig. 10a). Further magnified image (Fig. 10b) indicates that it is mainly composed of voluminous tiny erect flakes, which looks like the morphology of $Mg(OH)_2$ film reported.[59] EDS analysis in Fig. 10(c) indicates that the film composition is mainly Mg and O elements. The above results confirm that the corrosion film of Mg–6Ho binary alloy is mainly $Mg(OH)_2$ film. This loose and porous $Mg(OH)_2$ film provides limited protection to further corrosion underneath. However, for Mg–6Ho–0.5Zn alloy, both the morphology and the composition of corrosion film are dramatically different from these of Mg–6Ho alloy. As shown is Fig. 10(d), a very smooth and compact film is found on the surface of Mg–6Ho–0.5Zn alloy, in which the cracks are actually caused by dehydration of the layer during the drying process and under the vacuum of the SEM chamber. EDS analysis indicates that except for Mg and O, high contents of P, Ca and Ho are also detected in the corrosion layer, revealing the formation of hydroxides and hydroxyapatite corrosion product film. We consider that this is related with the compactness and stability of film layer for Mg–6Ho–0.5Zn, and finally may be attributed to the formation of SFs in microstructure. For Mg–6Ho–1.5Zn alloy, a thick and white corrosion film is visible to the naked eyes, which agrees with its high corrosion rate. As shown in Fig.

10(g), EDS analysis indicates that the composition of corrosion film is mainly Mg and O elements.

In view of the significant difference of corrosion films detected by SEM, further detection work was done to confirm the film composition of Mg–6Ho–0.5Zn alloy. Fig. 11 shows the XRD pattern of corrosion product powders stripped from the surface of Mg–6Ho–0.5Zn alloy after 10 days immersion in SBF. Besides the diffraction peaks from $Mg(OH)_2$, the diffraction peaks of $Ca_5(PO_4)_3(OH)$ and $Ho(OH)_3$ are also detected. As shown in Fig. 12, Mg (1s), O (1s), Ca (2p), P (2p), Ho (5p) are detected from the corrosion film of Mg–6Ho–0.5Zn alloy by XPS analyses. It is known

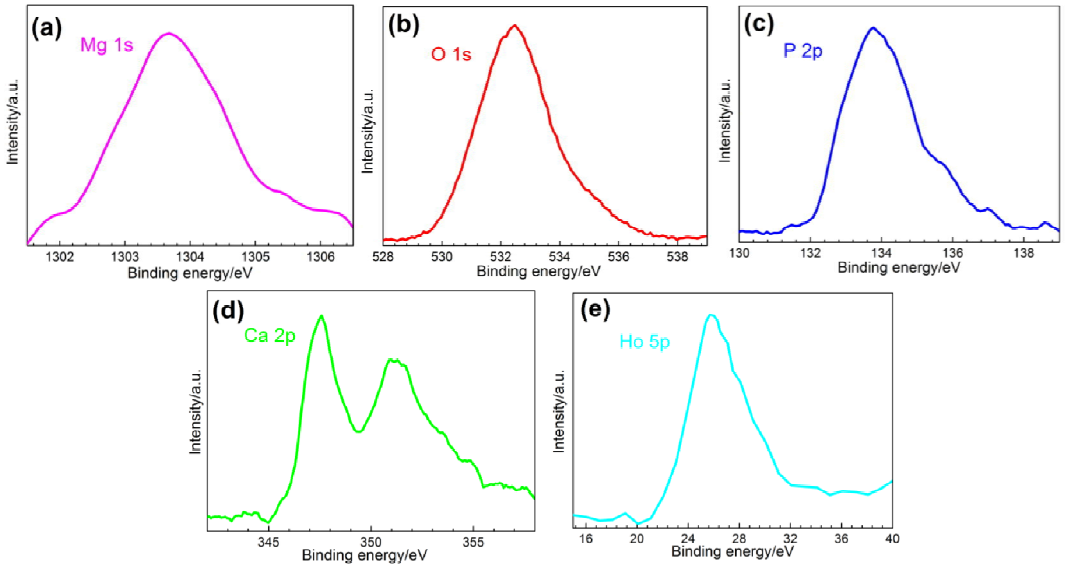

Fig. 12 XPS analyses of the corrosion product layer of Mg–6Ho–0.5Zn alloy after 10 days static immersion in SBF solution.

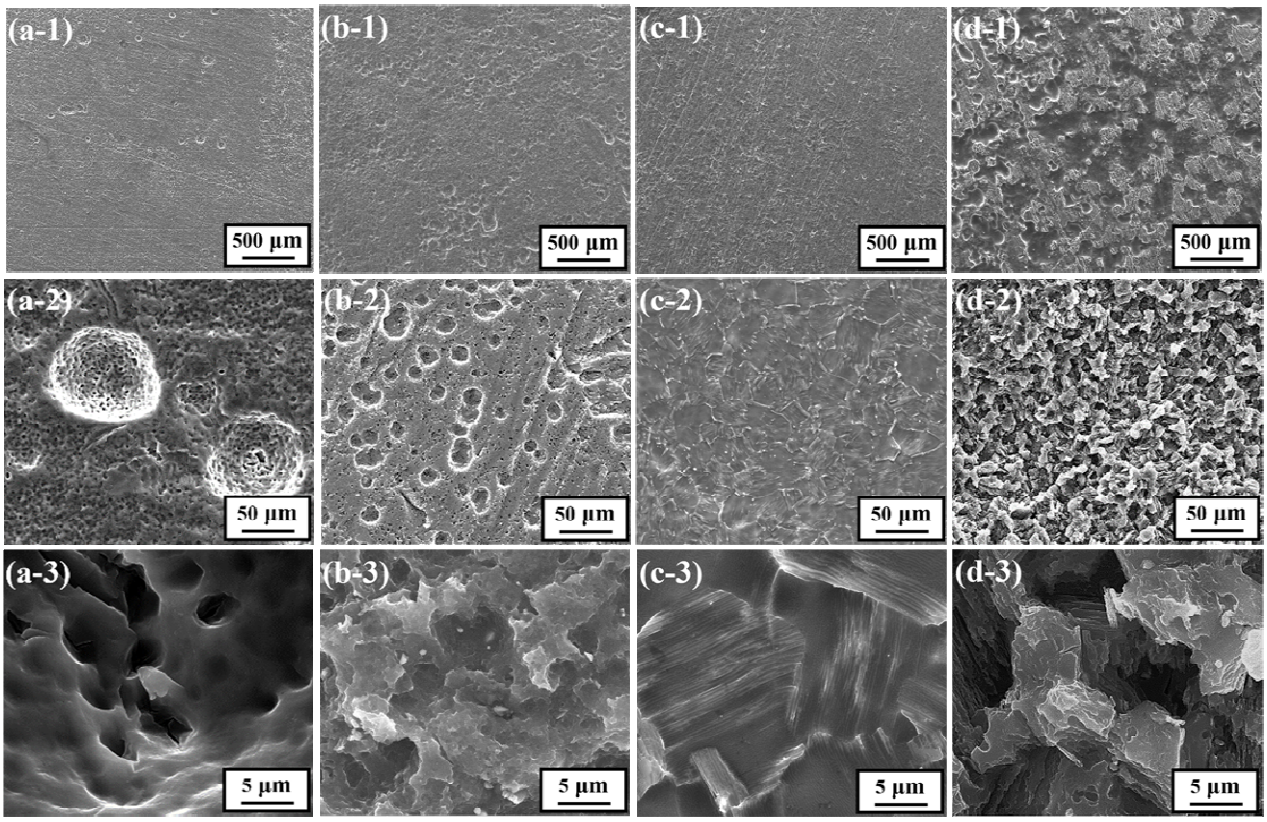

Fig. 13 SEM images of (a) pure Mg, (b) Mg–6Ho, (c) Mg–6Ho–0.5Zn and (d) Mg–6Ho–1.5Zn alloys after in vivo corrosion for 10 days and removing the corrosion products.

that the positions of the O 1s peak observed at 531.2 eV and 533.5 eV are corresponding to the OH^- and PO_4^{3-}, respectively. In addition, it also can be confirmed the element P exists in the film in a form of PO_4^{3-} from the binding energies of P 2p and Ca 2p. Thus, we can also deduce that $Mg(OH)_2$, $Ca_5(PO_4)_3(OH)$ and $Ho(OH)_3$ form the corrosion product film from XPS results, which is well consistent with the conclusion from XRD pattern.

Journal Name

ARTICLE

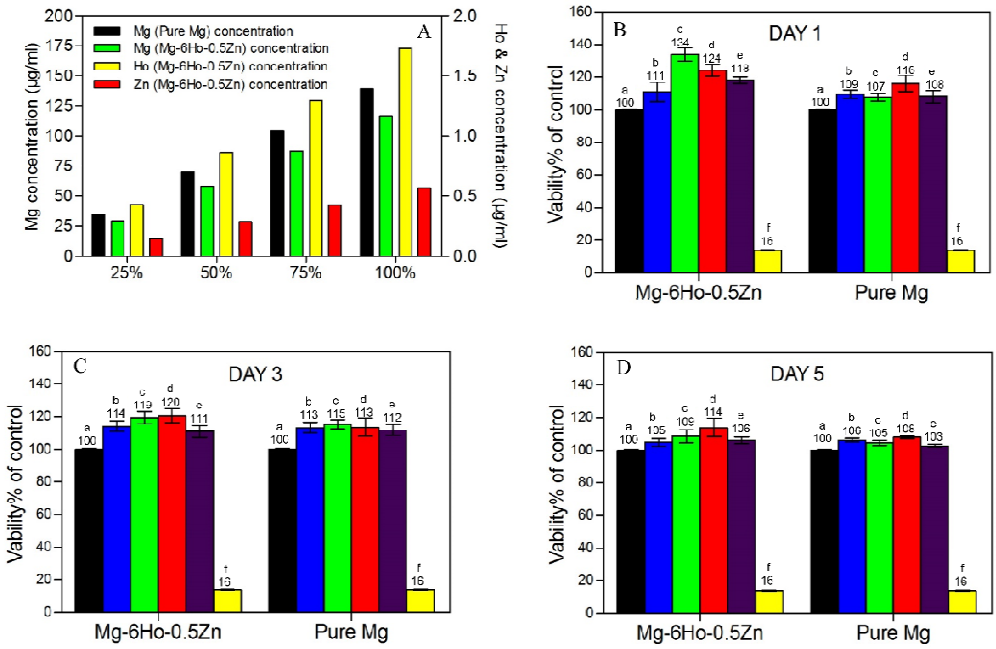

Fig. 14 (A) Ion concentration of Mg, Ho ang Zn released in extraction media. Saos-2 cell viability expressed as a percentage of the viability of cells in the control of culture in pure Mg and Mg-6Ho-0.5Zn alloy extraction media with (b) 25%, (c) 50%, (d) 75% and (e) 100% concentrations after (B) 1, (C) 3 and (D) 5 days ((a) is the blank negative control group (RPMI-1640 medium which does not include any extraction); (f) is the positive control group (0.64% phenol RPMI-1640 medium)).

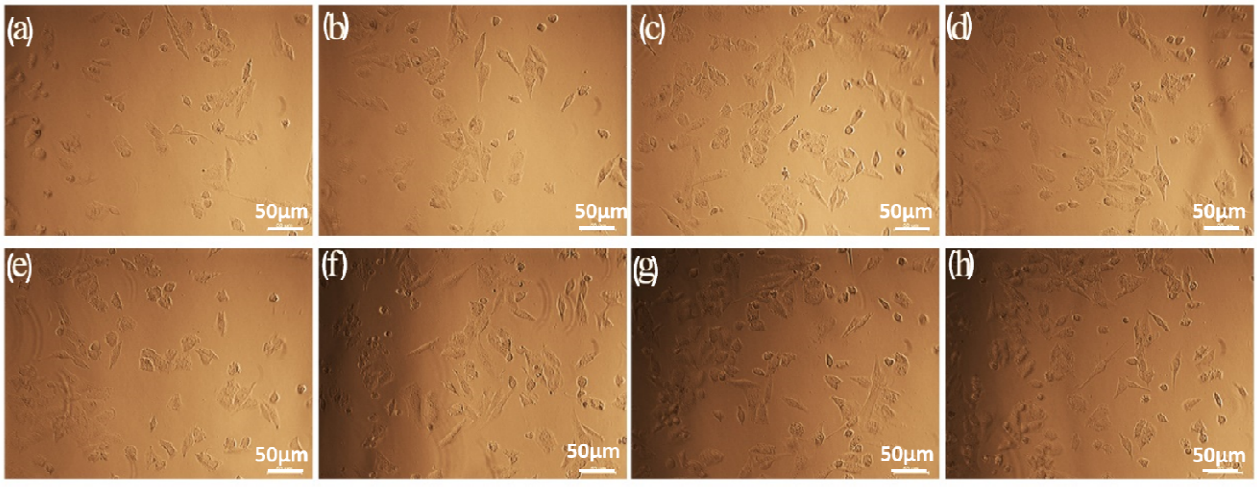

Fig. 15 Optical morphologies of Saos-2 cells cultured for 5 days of Mg–6Ho–0.5Zn alloy in (a) 25%, (b) 50%, (c) 75% and (d) 100% extracts and pure Mg in (e) 25%, (f) 50%, (g) 75% and (h) 100% extracts.

3.6. In vivo corrosion of Mg alloy with SFs

Witte et al.[8] have investigated the in vitro and in vivo corrosion behavior of AZ91D and LAE442 alloys, and their results indicate that the conclusion drawn from in vitro corrosion tests can not predict in vivo corrosion very well, though at present most of the researchers use in vitro corrosion measurement to evaluate the bio–corrosion behavior of Mg alloys. Furthermore, Walker et al.[60] proposed that predicting in vivo corrosion with in vitro immersion testing would be influenced by the various in vitro environments (solutions) and they considered that Earle's balanced salt solution (EBSS) could be used as a predictor of in vivo corrosion. In vivo corrosion of pure Mg and Mg–6Ho–0.5Zn alloy were also preliminarily tested in this work. Fig. 13 shows the surface morphologies of pure Mg and three alloys after being implanted in erector spinae of rabbit for 10 days and removed the corrosion products. For pure Mg sample (Fig. 13a1-a3), although the corrosion surface in most regions is flat, some occasional corrosion pits can also be observed. While by comparison, it is clear that more corrosion pits exist on the surface of Mg-6Ho alloy (Fig.13b VS Fig. 13a), and the most sever corrosion pits occurs on the surface of Mg-6Ho-1.5Zn alloy (Fig. 13d VS Fig. 13a and Fig.13b). In summary, the main in vivo corrosion mode for the above materials is pitting corrosion. However, compared the surface of Mg-6Ho-0.5Zn alloy with those of the above three materials, uniform in vivo corrosion feature can be observed clearly whether from low or high magnified images (Fig. 13c1-c3), which is as same as the corrosion mode in vitro environment. In addition, the visible polishing traces on both the flat corrosion matrix (Fig. 13c1) suggest that the corrosion is slighter than that in SBF for 10 days. Moreover, the corrosion film compositions for the alloys are similar as those in SBF for 10 days analyzed by SEM-EDS.

3.7. Cytocompatibility of the alloy with SFs

As a new designed degradable Mg–based implant material, it is essential to have accepted biocompatibility. Although some researchers generally believe that REs are not only non–toxic but also even anti–carcinogenic,[61-63] the biosafety of RE elements is still under concern.[7] In order to know the relationship between the ion concentration and the cellular response, the ion concentration of Mg, Ho and Zn released in extraction media after 1 day immersion is shown in Fig. 14(A). Fig. 14(B)-(D) show the Saos-2 cells viability cultured in 25%, 50%, 75% and 100% extraction medium of pure Mg and Mg-6Ho-0.5Zn alloy for 1, 3 and 5 days, respectively. It can be seen that cells cultured in pure Mg and Mg–6Ho–0.5Zn alloy extracts shows a significant higher viability than the negative and positive control groups. Furthermore, it should be noted that in almost all cases the cell viability of Mg–6Ho–0.5Zn alloy is better than that of pure Mg. In this study, there is no obvious relationship between the cell viability and ion concentration. Fig. 15 shows the morphologies of Saos-2 cells cultured in Mg-6Ho-0.5Zn and pure Mg extracts for 5 days. All the results for 25%, 50%, 75% and 100% extraction media exhibit a healthy morphology of cells with round and spindle shapes. The above results suggest that Mg–6Ho–0.5Zn alloy with SFs has the good biocompatibility and basic biosafety for biomedical application. The test result of low cytotoxicity of adding
Ho is consistent with previous results that the heavy REs, Dy and Gd with high solubility, exhibit low cytotoxicity and are suitable for biomedical magnesium alloys.[64]

4. Discussion

In this work, we report a novel Mg–Ho–Zn alloy with profuse basal plane SFs, and the alloy exhibits not only low bio–corrosion rate but also uniform corrosion mode on the premise of high mechanical properties.

4.1. High mechanical properties and formability

The mechanical test results demonstrate that Mg–6Ho–0.5Zn alloy possesses qualified mechanical properties as biomaterial (Table 3).[51] The formation of profuse SFs plays an important role in improving the mechanical properties. According to the TEM observation by Jian et al.,[65] under the applied stress, SFs would block dislocation slip and dislocations would cut SFs. Consequently, the interaction could increase the yield strength. Moreover, SFs could improve strain hardening and contribute to retain ductility by accumulating dislocations. In addition, EBSD analyses (Fig. 5) indicate the binary Mg–6Ho alloy has high basal slip Schmid factor, which would give a strong contribution to the high ductility. While in contrast, for Mg–6Ho–0.5Zn alloy, the relatively low basal slip Schmid factor would contribute to the high strength. On the other hand, the formation of SFs in Mg–6Ho–0.5Zn alloy almost does not
change the weak and random basal texture (Fig. 5f and g), suggesting weak anisotropy and relatively good secondary formability of Mg–6Ho–0.5Zn alloy material.

4.2. Original mechanism related to uniform corrosion and low corrosion rate

The high corrosion performance of Mg–6Ho–0.5Zn alloy is closely associated with the new microstructure and the corrosion surface layer. It is well known that microstructure plays an important role in the corrosion performance of materials.[33,39,40,43,66] Compared with common Mg alloys, the special microstructure of Mg–6Ho–0.5Zn alloy is basal plane SFs instead of intermetallic phases. Thus the formation of SFs is mainly responsible for the desirable corrosion behavior.

Firstly, the special effect of SFs on corrosion performance is attributed to their structure and composition. It is very common that intermetallic phase (including secondary phase and precipitate) acts as a potent local cathode in Mg alloys and micro–galvanic coupling would be built up between the intermetallic and the Mg matrix, which result in the preferential corrosion of Mg matrix surrounded the intermetallic (as seen in Fig. 8d and Fig. 9f).[67,68] However, SFs in Mg–6Ho–0.5Zn alloy are fundamentally different from those intermetallics. On the one hand, SFs are not intermetallic compounds but just the planar crystal lattice defects of Mg solid solution. As the defects, the energy and activity of SFs are higher than those of the perfect crystal (Mg). On the other hand, SFs contain little more Zn and Ho than Mg matrix, and the electrochemical potentials of element Zn and Ho are –0.76V and –

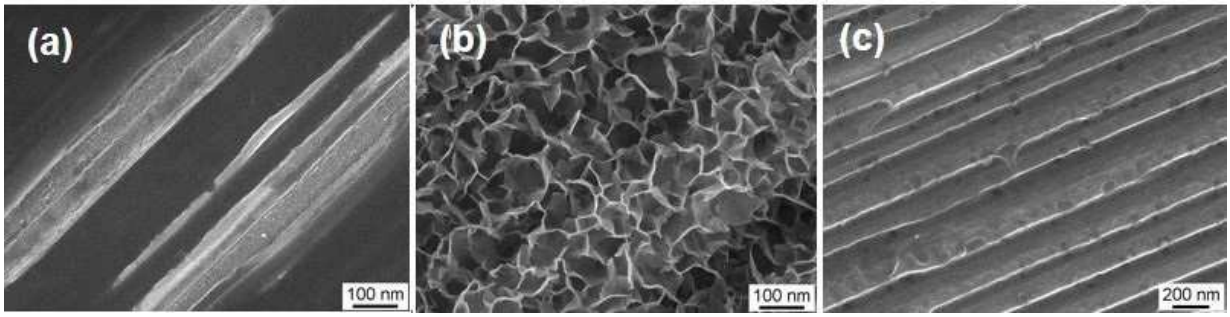

Fig. 16 SEM images of surface morphology of Mg–6Ho–0.5 alloy after immersion in SBF for (a) 10 min and (b) 30 min without removing the corrosion products; (c) SEM image of surface morphology of Mg–6Ho–0.5 alloy after immersion in SBF for 30 min and then removing the corrosion products.

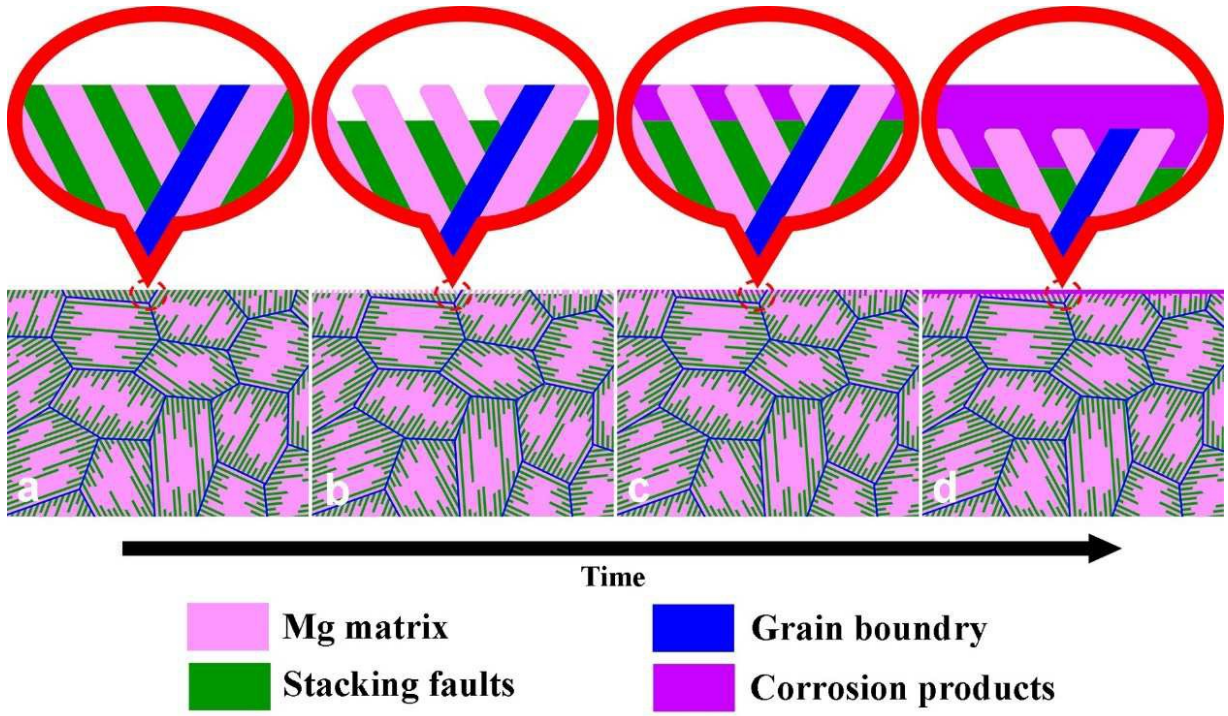

Fig. 17 a-d Schematic diagram of bio–corrosion process for Mg–6Ho–0.5Zn alloy with SFs. It demonstrates that the high corrosion performance is closely associated with the SFs and the quickly effective corrosion surface layer.

2.33V, which are positive compared with that of Mg (–2.37V). Therefore, it is deduced that SFs may act as weak anode rather than cathode or strong anode, and SFs are preferentially corroded compared with Mg matrix. In other word, SFs as sacrificial anode would display protective effect on Mg matrix. The deduction is confirmed by the experimental observation. Fig. 16(a) shows the corroded surface of Mg–6Ho–0.5Zn alloy sample immersed in SBF for a short time of 10 min. It can be seen that SFs are corroded but the Mg matrix seems to be virtually undamaged. More interestingly, the SFs location forms compact corrosion product layer which can prevent further corrosion attack effectively. When the immersion time is up to 30 min, the corrosion product layer extends to full surface of the alloy sample, as shown in Fig. 16(b). But the parallel and shallow grooves on the surface after removing the corrosion products (Fig. 16c) still reveal the preferential corrosion of SFs and the protected Mg matrix. Therefore, we first report that the novel SFs in Mg alloy display essential difference in the role of bio–corrosion compared with intermetallics.

Secondly, the small size of SFs plays a positive role in improving the corrosion performance. Yang et al.[33] reported that the cathode–to–anode area was an effect factor on the tendency of local micro–galvanic corrosion, and the nano–sized precipitates in the aged Mg–Dy–Gd–Zr alloys could largely decrease the local

micro galvanic corrosion compared with the micro–sized second–phase particles in the as–cast Mg–Dy–Gd–Zr alloys. In the current study, SFs in as–extruded Mg–6Ho–0.5Zn alloy are one–dimensional nanostructure.[48] Therefore, single cathode–to–anode area in Mg–6Ho–0.5Zn alloy is very small. Accordingly, the small size of SFs is also beneficial for slowing down corrosion rate as well as corrosion mode.

The last but not the least, the uniform corrosion mode is also related to the morphology and distribution of SFs. SFs have one–dimensional nanostructure, which can be regarded approximately as nanowires, and the spacing of SFs ranges just from tens of nanometers to about 300 nanometers (Fig. 3a). Furthermore, SFs are parallel in a α–Mg grain, and they have different orientation in different grains (Fig. 2b and e). All above features of SFs destine that the corrosion expands preferentially along the SFs length direction in the interior of a α–Mg grain and the Mg matrix around SFs acts as the protected object (Fig. 16a and c), and meanwhile it is difficult for the corrosion to extend to the neighboring grains further due to the different orientation of SFs in different grains (Fig. 8c). Finally, uniform corrosion mode and low corrosion rate are realized in Mg–6Ho–0.5Zn alloy with SFs.

Besides the microstructure, the protective corrosion film on the surface is another reason for the low corrosion rate of Mg–6Ho–0.5Zn alloy. It is well known that pure $Mg(OH)_2$ film is not compact and easily disrupted in chloride solutions,[69,70] but the corrosion film of Mg–6Ho–0.5Zn alloy seems to be compact and stable relatively (Fig. 10d). More importantly, the film is found to have a complex composition, which contains $Mg(OH)_2$, $Ho(OH)_3$ and $Ca_5(PO_4)_3(OH)$. The solubility products constant (Ksp) for $Ho(OH)_3$ is much smaller than that of $Mg(OH)_2$, thus the formation of $Ho(OH)_3$ can improve the stability of surface film.[32,70,71] In addition, the high content Ho^{3+} in the hydroxide film structure is considered to be able to increase the local positive charge, which can reduce the penetration of detrimental anions (Cl^-) across the corrosion film by trapping anions, and hence further inhibit corrosion.[69] On the other hand, $Ca_5(PO_4)_3(OH)$ is an essential component in bone, and therefore Mg–6Ho–0.5Zn alloy with $Ca_5(PO_4)_3(OH)$ formed on the surface would have a good biocompatibility when it is used as biodegradable material within bone.

According to the experimental results, it can be confirmed that corrosion mechanism of the alloy with SFs is very different from the common Mg alloys, and the proposed corrosion mechanism in the Mg–6Ho–0.5Zn alloy is shown schematically in Fig. 17. SFs act as weak anode to avoid the Mg matrix corrosion preferentially and inhibit corrosion extension effectively. Moreover, the promptly effective formation of corrosion product film further results in lower corrosion rate and more uniform corrosion behavior.

5. Conclusions

In this work, a new microstructure has been proposed to design biodegradable Mg alloy with desired performance. The main results are summarized as follows.

(1) Profuse nano–spaced basal plane SFs can be obtained in the Mg–6Ho–0.5Zn alloy through a combination of direct–chill semi–continuous casting, heat–treatment and hot–extrusion.

(2) Benefiting from the formation of SFs, the Mg–6Ho–0.5Zn alloy exhibits high in vitro and in vivo corrosion properties, including uniform corrosion behavior and low corrosion rate along with high mechanical properties and acceptable cytotoxicity.

(3) The unique effect of SFs on bio–corrosion properties is quite different from the common intermetallic particles. An original uniform corrosion mechanism is firstly proposed based on the special defect structure,orientation of SFs and prompt effective corrosion film.

Acknowledgments

This work was supported by National Natural Science Foundation of China (51301048, 51171081, and 51371062), the Fundamental Research Funds for the Central Universities (HEUCFZ1308), NSFHLJ (ZD201411), the Project for Innovative Talents of Science and Technology of Harbin (2014RFXXJ006), and the Project 2013DB04 at NPL, CAEP.

References

1 M. P. Staiger, A. M. Pietak, J. Huadmai and G. Dias, *Biomaterials*, 2006, **27**, 1728–1734.
2 Y. F. Zheng, X. N. Gu and F. Witte, *Mater. Sci. Eng., R*, 2014, **77**, 1–34.
3 Y. F. Ding, C. E. Wen, P. Hodgson and Y. C. Li, *J. Mater. Chem. B*, 2014, **2**, 912–1933.
4 J. Walker, S. Shadanbaz, T. B. F. Woodfield, M. P. Staiger and G. J. Dias, *J. Biomed. Mater. Res., Part B*, 2014, **102B**, 1316–1331.
5 X. N. Gu, Y. F. Zheng, Y. Cheng, S. P. Zhong and T. F. Xi, *Biomaterials*, 2009, 30, 484–498.
6 Y. J. Chen, Z. G. Xu, C. Smith and J. Sankar, *Acta Biomater.*, 2014, **10**, 4561–4573.
7 N. Li and Y. F. Zheng, *J. Mater. Sci. Technol.*, 2013, **29**, 489–502.
8 F. Witte, J. Fischer, J. Nellesen, H.A. Crostack, V. Kaese, A. Pisch, F. Beckmann and H. Windhagen, *Biomaterials*, 2006, **27**, 1013–1018.
9 G. L. Song, *Corros. Sci.*, 2007, **49**, 1696–1701.
10 W. Zhou, T. Shen and N. N. Aung, *Corros. Sci.*, 2010, **52**, 1035–1041.
11 L. Mao, G. Yuan, S. Wang, J. Niu, G. Wu and W. Ding, *Mater. Lett.*, 2012, **88**, 1–4.
12 M. B. Kannan and R. K. S. Raman, *Biomaterials*, 2008, **29**, 2306–2314.
13 J. Hofstetter, E. Martinelli, A. M. Weinberg, M. Becker, B. Mingler, P.J. Uggowitaer and J.F. Löffler, *Corros. Sci.*, 2015, **91**, 29–36.
14 N. I. Z. Abidin, B. Rolfe, H. Owen, J. Malisano, D. Martin, J. Hofstetter, P.J. Uggowitzer and A. Atrens, *Corros. Sci.*, 2013, **75**, 354–366.
15 Q. M. Peng, Y. D. Huang, L. Zhou, N. Hort and K.U. Kainer, *Biomaterials*, 2010, **31**, 398–403.
16 Z. J. Li, X. N. Gu, S. Q. Lou and Y. F. Zheng, *Biomaterials*, 2008, **29**, 1329–1344.
17 Y. S. Jeong and W. J. Kim, *Corros. Sci.*, 2014, **82**, 392–403.
18 S. Zhang, X. Zhang, C. Zhao, J. Li, Y. Song, C. Xie, H. Tao, Y. Zhang, Y. He, Y. Jiang and Y. Bian, *Acta Biomater.*, 2010, **6**, 626–640.
19 Q. Peng, X. Li, N. Ma , R. Liu and H. Zhang, *J. Mech. Behav. Biomed. Mater.*, 2012, **10**, 128–137.
20 X. N. Gu, X. H. Xie, N. Li, Y. F. Zheng and L. Qin, *Acta Biomater.*, 2012, **8**, 2360–2374.

21 Y. F. Ding, Y. C. Li, J. X. Lin and C. E. Wen, *J. Mater. Chem. B*, 2015, **3**, 3714–3729.
22 W. R. Zhou, Y. F. Zheng, M. A. Leeflang and J. Zhou, *Acta Biomater.*, 2013, **9**, 8488–8498.
23 L. L. Tan, X. M. Yu, P. Wan and K. Yang, *J. Mater. Sci. Technol.*, 2013, **29**, 503–513.
24 H. Hermawan, D. Dubé and D. Mantovani, *Acta Biomater.*, 2010, **6**, 1693–1697.
25 B. Smola, L. Joska, V. Březina, I. Stulíková and F. Hnilica, *Mater. Sci. Eng., C*, 2012, **32**, 659–664.
26 H. S. Brar, J. P. Ball, I. S. Berglund, J. B. Allen and M. V. Manuel, *Acta Biomater.*, 2013, **9**, 5331–5340.
27 D. T. Chou, D. Hong, P. Saha, J. Ferrero, B. Lee, Z. Tan, Z. Dong and P. N. Kumta, *Acta Biomater.*, 2013, **9**, 8518–8533.
28 N. Hort, Y. Huang, D. Fechner, M. Störmer, C. Blawert, F. Witte, C. Vogt, H. Drücker, R. Willumeit, K.U. Kainer and F. Feyerabend, *Acta Biomater.*, 2010, **6** 1714–1725.
29 L. Yang, N. Hort, D. Laipple, D. Höche, Y. Huang, K. U. Kainer, R. Willumeit and F. Feyerabend, *Acta Biomater.*, 2013, **9**, 8475–8487.
30 L. Yang, Y. Huang, F. Feyerabend, R. Willumeit, C. Mendis, K. U. Kainer and N. Hort, *Acta Biomater.*, 2013, **9**, 8499–8508.
31 J. M. Seitz, R. Eifler, J. Stahl, M. Kietzmann and F. W. Bach, *Acta Biomater.*, 2012, **8**, 3852–3864.
32 A. C. Hänzi, I. Gerber, M. Schinhammer, J. F. Löffler and P. J. Uggowitzer, *Acta Biomater.*, 2010, **6**, 1824–1833.
33 J. Fan, X. Qiu, X. Niu, Z. Tian, W. Sun, X. Liu, Y. Li, W. Li and J. Meng, *Mater. Sci. Eng., C*, 2013, **33**, 2345–2352.
34 X. Zhao, L. L. Shi and J. Xu, *J. Mech. Behav. Biomed. Mater.*, 2013, **18**, 181–190.
35 Z. Leng, J. Zhang, T. Yin, L. Zhang, X. Guo, Q. Peng, M. Zhang and R. Wu, *J. Mech. Behav. Biomed. Mater.*, 2013, **28**, 332–339.
36 X. Zhang, Z. Ba, Q. Wang, Y. Wu, Z. Wang and Q. Wang, *Corros. Sci.*, 2014, **88**, 1–5.
37 X. Zhang, Y. Wu, Y. Xue, Z. Wang and L. Yang, *Mater. Lett.*, 2012, **86**, 42–45.
38 Q. Peng, J. Guo, H. Fu, X. Cai, Y. Wang, B. Liu and Z. Xu, *Sci. Rep.*, 2014, **4**, 3620; DOI: 10.1038/srep03620.
39 Y. Liao, Y. Ouyang, J. Niu, J. Zhang, Y. Wang, Z. Zhu, G. Yuan, Y. He and Y. Jiang, *Mater. Lett.*, 2012, **83**, 206–208.
40 L. Yang, Y. Huang and Q. Peng, *Mater. Sci. Eng., B*, 2011, **176**, 1827–1834.
41 X. H. Zhou, Y. W. Huang, Z. l. Wei, Q. R. Chen and F. X. Gan, *Corros. Sci.*, 2006, **48**, 4223-4233.
42 T. Yoshida, K. Itoh, R. Tamura and S. Takeuchi, *Mater. Sci. Eng., A*, 2000, **294-296**, 786-789.
43 B. Z. Liu, J. J. Liu, X. L. Hou, Z. Zhang, L. Li and L. M. Wang, *Trans. Nonferrous Met. Soc. China*, 2010, **20**, s346-s351.
44 M. Liu, P. J. Uggowitzer, A. V. Nagasekhar, P. Schmutz, M. Easton, G. L. Song and A. Atrens, *Corros. Sci.*, 2009, **51**, 602–619.
45 M. C. Zhao, P. Schmutz, S. Brunner, M. Liu, G. L. Song and A. Atrens, *Corros. Sci.*, 2009, **51**, 1277–1292.
46 Z. M. Shi, M. Liu and A. Atrens, *Corros. Sci.*, 2010, **52**, 579–588.
47 J. Wang, X. Zhu, R. Wang, Y. Xu, J. Nie and G. Ling, *J. Rare Earth.*, 2011, **29**, 454–459.
48 S. D. Wang, D. K. Xu, X. B. Chen, E. H. Han and C. Dong, *Corros. Sci.*, 2015, **92**, 228–236.
49 K. Liu, J. Zhang, H. Lu, D. Tang, L. L. Rokhlin, F. M. Elkin and J. Meng, *Mater. Des.*, 2010, **31**, 210–219.
50 Q. Wang, K. Liu, Z. Wang, S. Li and W. Du, *J. Alloys Compd.*, 2014, **602**, 32–39.
51 M. Yamasaki, M. Sasaki, M. Nishijima, K. Hiraga and Y. Kawamura, *Acta Mater.*, 2007, **55**, 6798–6805.
52 A. Atrens, G. L. Song, M. Liu, Z. Shi, F. Cao, and M. S. Dargusch, *Adv. Eng. Mater.*, 2015, **17**, 400–453.
53 N. Ma, Q. Peng, J. Pan, H. Li and W. Xiao, *J. Alloys Compd.*, 2014, **592**, 24–34.
54 M. Erinc, W. H. Sillekens, G. Mannens and R. Werkhoven, Magnesium Technology (2009), New York: TMS, 209–214.
55 G. Song and A. Atrens, *Adv. Eng. Mater.*, 2003, **5**, 837–858.
56 Z. Shi and A. Atrens, *Corros. Sci.*, 2011, **53**, 226–246.
57 S. Izumi, M. Yamasaki and Y. Kawamura, *Corros. Sci.*, 2009, **51**, 395–402.
58 M. Liu, P. Schmutz, P. J. Uggowitzer, G. Song and A. Atrens, *Corros. Sci.*, 2010, **52**, 3687–3701.
59 J. Zhang, X. Niu, X. Qiu, K. Liu, C. Nan, D. Tang and J. Meng, *J. Alloys Compd.*, 2009, **471**, 322–330.
60 J. Walker, S. Shadanbaz, N. T. Kirkland, E. Stace, T. Woodfield, M. P. Staiger and G. J Dias, *J. Biomed. Mater. Res. Part. B*, 2012, **100B**, 1134–1141.
61 F. Witte, N. Hort, C. Vogt, S. Cohen, K. U. Kainer, R. Willumeit and F. Feyerabend, *Curr. Opin. Solid State Mater. Sci.*, 2008, **12**, 63–72.
62 W. D. Yang, P. Zhang, J. S. Liu and Y. F. Xue, *J. Rare Earth.*, 2006, **24**, 369–373.
63 R. K. S. Raman, S. Jafari and S. E. Harandi, *Eng. Fract. Mech.*, 2015, **137**, 97–108.
64 F. Feyerabend, J. Fischer, J. Holtz, F. Witte, R. Willumeit, H. Drücker, C. Vogt and N. Hort, *Acta Biomater.*, 2010, **6**, 1834–1842.
65 W. W. Jian, G. M. Cheng, W. Z. Xu, H. Yuan, M. H. Tsai, Q. D. Wang, C. C. Koch, Y. T. Zhu and S. N. Mathaudhu, *Mater. Res. Lett.*, 2013, **1**, 61–66.
66 Y. Lu, A. R. Bradshaw, Y. L. Chiu and I. P. Jones, *J. Alloys Compd.*, 2014, **614**, 345–352.
67 G. Song and A. Atrens, *Adv. Eng. Mater.*, 1999, **1**, 11–33.
68 G. Song and A. Atrens, *Adv. Eng. Mater.*, 2003, **5**, 837–858.
69 H. B. Yao, Y. Li, A. T. S. Wee, J. S. Pan and J. W. Chai, *Appl. Surf. Sci.*, 2001, **173**, 54–61.
70 R. Pinto, M. G. S. Ferreira, M. J. Carmezim and M. F. Montemor, *Electrochim. Acta*, 2011, **56**, 1535–1545.
71 Y. L. Song, Y. H. Liu, S. H. Wang, S. R. Yu and X. Y. Zhu, *Mater. Corros.*, 2007, **58**, 189–192.